Fast and Accurate Imaging Algorithm for Targets Buried in Dielectric Medium for UWB Radars

Ken AKUNE, *Shouhei KIDERA*, and *Tetsuo KIRIMOTO*
Graduate School of Informatics and Engineering, University of Electro-Communications,
Tokyo, Japan.
Email: akune@secure.ee.uec.ac.jp

Abstract

Ultra-wide band (UWB) pulse radar with high range resolution and dielectric permeability is promising as an internal imaging technique for non-destructive testing or breast cancer detection. Various imaging algorithms for UWB radar techniques have been proposed, such as aperture synthesis and the space-time beamforming algorithm. However, these algorithms are based on a signal focusing scheme, which often suffers from insufficient resolution to identify the detailed structure of buried targets and has high computational cost in obtaining a full three-dimensional image. To overcome these difficulties, this paper proposes an accurate fast imaging algorithm for targets buried in a uniform dielectric medium by advancing the RPM(Range Points Migration) algorithm, which has been shown to achieve super-resolution imaging for spatial measurement. Numerical simulation shows that the proposed algorithm achieves imaging accuracy of around $1/20\ \lambda$ with less computation time by specifying boundary extraction.

1 Introduction

UWB pulse radar has great potential to reconstruct objects buried in a human body or concrete wall while avoiding harm to human tissue or communication systems. It thus has various applications such as the early-stage detection of breast tumors, non-destructive testing to find cracks in pipes within walls, and positioning of unexploded land mines in the subsurface. Various imaging algorithms suitable for the above applications have been developed, such as synthetic aperture radar (SAR) and microwave imaging via space-time beamforming (MIST) algorithm [1]. However, these algorithms are based on signal integrations, and their spatial resolution is more than half the pulsewidth, even in the noiseless case, and they require large computational resources especially in the three-dimensional case. As a novel solution to these problems, this paper extends the principle of the former RPM algorithm to internal imaging, which realizes high-speed and super-resolution spatial imaging [2]. Our proposed algorithm efficiently employs dielectric boundary points and their normal vectors preliminary obtained by RPM, and accurately extracts the target boundary points employing the advanced RPM principle and Snell's law if the relative permittivity of the dielectric medium is a known constant. Numerical simulation shows that our proposed algorithm has much better performance than the conventional SAR algorithm in accurate boundary extraction. It also remarkably decreases the computational burden because it directly maps the extracted range points to the target boundary points without integration.

2 System Model

Figure 1 shows the system model. We assume that a target and dielectric medium have arbitrary shape with clear boundaries. The relative permittivity of the dielectric medium is assumed to be a known constant. The propagation speed of the radio wave c in air is a known constant. A mono-static radar with an omni-directional antenna scans along the x-axis. A mono-cycle pulse is provided as a transmitting current. The real space in which the target and antenna are located is defined by parameters $\boldsymbol{r} = (x, z)$, and is normalized by the central wavelength λ of the transmitted pulse. $s(X, Z)$ is defined as the output of the Wiener filter at the antenna location $(X, 0)$, where $Z = ct/2\lambda$ is expressed by time t. A set of range points defined as $\mathcal{Q} \equiv \{\boldsymbol{q}_i = (X_i, Z_i), (i = 1, ...N_Q)\}$ is extracted from the local maxima of $s(X, Z)$ [2].

978-1-4244-6051-9/11/$26.00 ©2011 IEEE

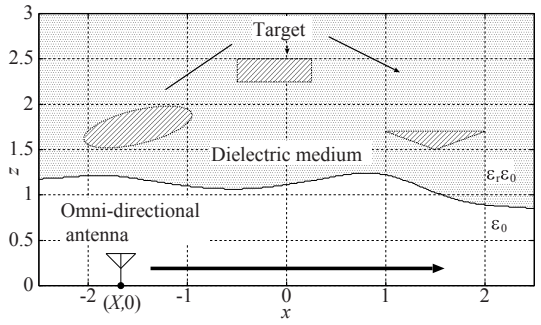

Figure 1: System model.

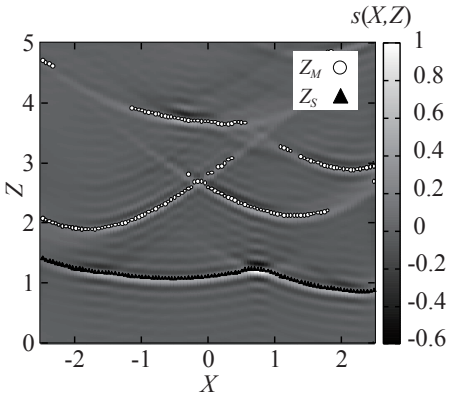

Figure 2: Output of the Wiener filter $s(X, Z)$, where the target as in Fig. 1 is assumed.

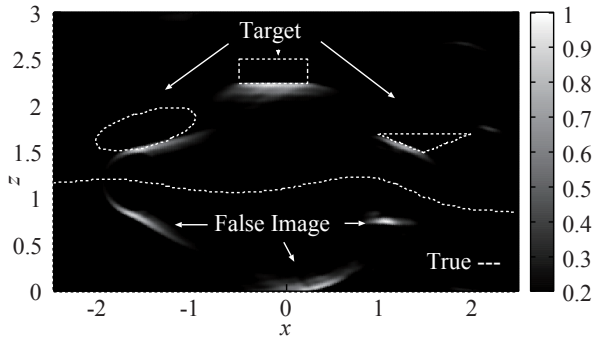

Figure 3: Estimated images with SAR algorithm in noiseless situation.

3 Conventional Algorithm based on SAR

This section describes the conventional imaging algorithm by extending SAR to internal imaging. This algorithm deals with the boundary points of the dielectric medium $\boldsymbol{r}_{S,j} = (x_{S,j}, z_{S,j})\,(j = 1, ..., N_S)$, preliminarily produced by the RPM algorithm with a subset of $\mathcal{Q}$ denoted as $\mathcal{Q}_S \equiv \left\{\boldsymbol{q}_{S,j} = (X_{S,j}, Z_{S,j}), (j = 1, ..., N_S)\right\}$, with each member having a minimum Z for each antenna location. Each point $\boldsymbol{r}_{S,j}$ is regarded as a candidate for an incident point on the dielectric medium boundary. The SAR scheme is then readily extended to imaging of a target buried in the dielectric medium using RPM points. If the relative permittivity ϵ_r is known, the internal image $I(\boldsymbol{r})$ is formulated as

$$I(\boldsymbol{r}) = \int_{X\in\Gamma} \sum_{j=1}^{N_S'} s\left(\boldsymbol{q}_{S,j}\right) s\left(X, d_2\left(X, \boldsymbol{r}, \boldsymbol{r}_{S,j}\right)\right) \mathrm{d}X, \tag{1}$$

where $d_2(X, \boldsymbol{r}, \boldsymbol{r}_{S,j}) = \sqrt{(X - x_{S,j})^2 + {z_{S,j}}^2} + \sqrt{\epsilon_r}\sqrt{(x - x_{S,j})^2 + (z - z_{S,j})^2}$ and Γ denotes the spatial range of the antenna scanning. $\boldsymbol{r}_{S,j}$ is interpolated with a cubic spline function, and the interpolation increases the number of boundary points to N_S'. In Eq. (1), $\boldsymbol{r}_{S,j}$ is regarded as the incident points on the dielectric medium, and a buried target boundary is reconstructed by aperture synthesis considering the velocity degradation. Figure 2 shows an example of $s(X, Z)$ in the case illustrated in Fig. 1, where each signal is received at 101 locations for $-2.5 \le X \le 2.5$. The conductivity of each target is set to 1.0×10^6S/m. The conductivity and relative permittivity of the dielectric medium are set to 1.0×10^{-2}S/m and $\epsilon_r = 5$, respectively. Figure 3 shows the image $I(\boldsymbol{r})$ obtained by this algorithm in the noiseless situation, which is normalized by the maximum value of $I(\boldsymbol{r})$. It is confirmed that while parts of the targets can be recon-

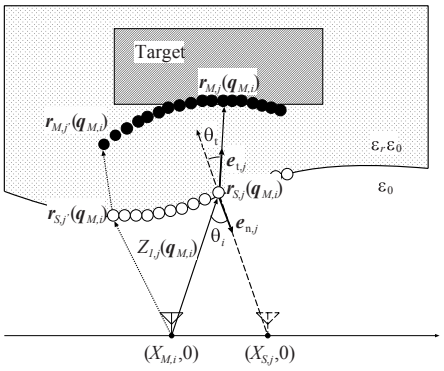

Figure 4: Relationship between the potential target points and the boundary points of the dielectric medium.

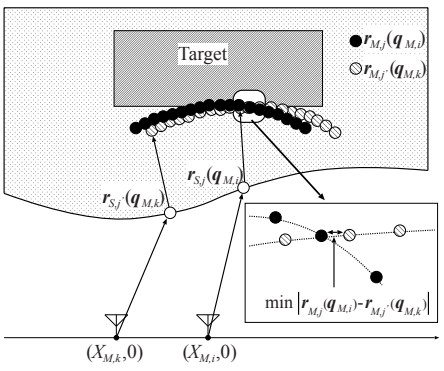

Figure 5: Relationship between the two groups of the candidate points $\boldsymbol{r}_{M,j}\left(\boldsymbol{q}_{M,i}\right)$ and $\boldsymbol{r}_{M,j'}\left(\boldsymbol{q}_{M,k}\right)$.

structed, undesirable false images are created outside the dielectric medium. Furthermore, the computational time is longer than 1300 s with a Xeon 2.40 GHz processor. Note that in the three-dimensional case, this computational cost becomes an enormous and is impractical for medical screening or non-destructive testing.

4 Proposed algorithm

To overcome the problems described above, this paper proposes a novel imaging algorithm for objects buried in a dielectric medium. The algorithm makes use of the inherent characteristic of the RPM algorithm, which provides not only accurate target points but also the normal vectors on their boundaries without a derivative operation. If a normal vector at each dielectric boundary point is given, the propagation path in its medium is automatically calculated using Snell's law. In fact, each normal vector on RPM boundary points $\boldsymbol{r}_{S,j}$ is calculated as $\boldsymbol{e}_{\mathrm{n},j} = \left(\left(X_{S,j} - x_{S,j}\right), -z_{S,j}\right)/Z_{S,j}$. Here, a set of all range points except $\mathcal{Q}_S$ is defined as $\mathcal{Q}_M = \mathcal{Q} \bigcap \overline{\mathcal{Q}_S} \equiv \left\{\boldsymbol{q}_{M,i} = \left(X_{M,i}, Z_{M,i}\right), (i = 1, ..., N_M)\right\}$. For each $\boldsymbol{r}_{S,j}$, the potential target points $\boldsymbol{r}_{M,j}\left(\boldsymbol{q}_{M,i}\right)$ corresponding to $\boldsymbol{q}_{M,i}$ are calculated:

$$\boldsymbol{r}_{M,j}\left(\boldsymbol{q}_{M,i}\right) = \boldsymbol{r}_{S,j} + \frac{\left(Z_{M,i} - Z_{1,j}\left(\boldsymbol{q}_{M,i}\right)\right)\boldsymbol{e}_{t,j}}{\sqrt{\epsilon_r}}, \tag{2}$$

where $Z_{1,j}\left(\boldsymbol{q}_{M,i}\right) = \sqrt{\left(X_{M,i} - x_{S,j}\right)^2 + z_{S,j}^2}$, $\boldsymbol{e}_{t,j} = R\left(\theta_t\right)\left(-\boldsymbol{e}_{\mathrm{n},j}\right)$ and $R\left(\theta\right)$ is a rotation matrix in the counterclockwise direction, and the refraction angle $\theta_t = \sin^{-1}\left(\sin\theta_i/\sqrt{\epsilon_r}\right)$. $\theta_i = \sin^{-1}\left(\boldsymbol{e}_{\mathrm{n},j} \times \boldsymbol{e}_{i,j}\right)$. Here, $\boldsymbol{e}_{i,j} = \left(\left(X_{M,i} - x_{S,j}\right), -z_{S,j}\right)/Z_{1,j}\left(\boldsymbol{q}_{M,i}\right)$. Figure 4 shows the relationship between the potential target points and the boundary points of the dielectric medium. The algorithm assumes that the target point exists in a set of $\boldsymbol{r}_{M,j}\left(\boldsymbol{q}_{M,i}\right)$ on the extended principle of the RPM [2]. To detect the actual target point corresponding to $\boldsymbol{q}_{M,i}$, the function $f\left(\boldsymbol{r}_{M,j}\left(\boldsymbol{q}_{M,i}\right), \boldsymbol{q}_{M,k}\right)$ is introduced:

$$f\left(\boldsymbol{r}_{M,j}\left(\boldsymbol{q}_{M,i}\right), \boldsymbol{q}_{M,k}\right) = \exp\left(-\frac{\min_{1\le j'\le N_S}\left|\boldsymbol{r}_{M,j}\left(\boldsymbol{q}_{M,i}\right) - \boldsymbol{r}_{M,j'}\left(\boldsymbol{q}_{M,k}\right)\right|^2}{2\sigma_r^2}\right), \tag{3}$$

where σ_r is an empirically determined constant. Figure 5 depicts the relationship between the two groups of the candidate points $\boldsymbol{r}_{M,j}\left(\boldsymbol{q}_{M,i}\right)$ and $\boldsymbol{r}_{M,j'}\left(\boldsymbol{q}_{M,k}\right)$. Any function with a central peak and symmetric curve, such as the raised cosine function, can be used in Eq. (3) instead of the Gaussian function. $f\left(\boldsymbol{r}_{M,j}\left(\boldsymbol{q}_{M,i}\right), \boldsymbol{q}_{M,k}\right)$ is a weight based on the minimum distance between $\boldsymbol{r}_{M,j}\left(\boldsymbol{q}_{M,i}\right)$ and all candidate points determined by $\boldsymbol{q}_{M,k}$. The target points for each $\boldsymbol{q}_{M,i}$ are calculated as

$$\hat{\boldsymbol{r}}_M\left(\boldsymbol{q}_{M,i}\right) = \underset{\boldsymbol{r}_{M,j}\left(\boldsymbol{q}_{M,i}\right)}{\arg\max}\left|\sum_{k=1}^{N_M} s\left(\boldsymbol{q}_{M,k}\right) f\left(\boldsymbol{r}_{M,j}\left(\boldsymbol{q}_{M,i}\right), \boldsymbol{q}_{M,k}\right)\exp\left(-\frac{\left|X_{M,i} - X_{M,k}\right|^2}{2\sigma_X^2} - \frac{\left|Z_{M,i} - Z_{M,k}\right|^2}{2\sigma_Z^2}\right)\right|, \tag{4}$$

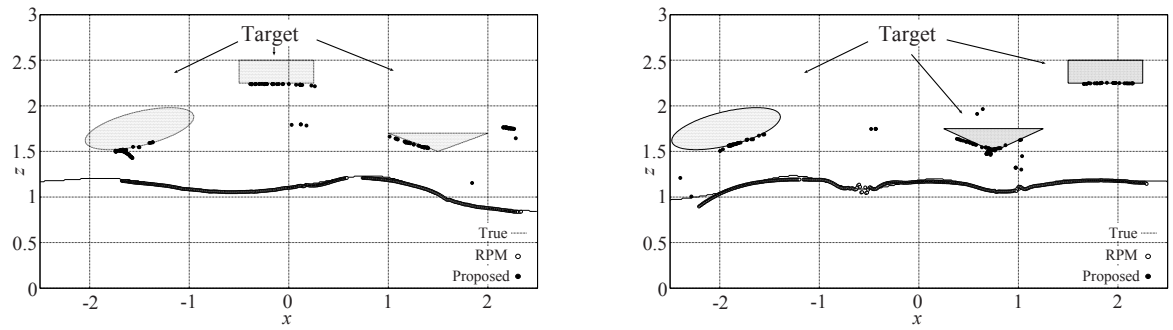

Figure 6: Estimated image with the proposed algorithm in noiseless situation (left:case(a), right:case(b)).

where σ_X and σ_Z are empirically determined constants. It is expected that the algorithm realizes accurate internal imaging by incorporating the principle of the RPM algorithm and Snell's law. In addition, the proposed algorithm remarkably decreases the computational burden, compared with the traditional SAR algorithm, by removing the integration process.

5 Simulation Results and Conclusions

This section presents examples of the proposed algorithm using numerical simulation. Figure 6(a) shows the target points estimated by RPM and the proposed algorithm. $\sigma_r = 0.5\lambda$, $\sigma_X = 1.25\lambda$, $\sigma_Z = 0.5\lambda$ are set. Here, the black dots denote the target points obtained by the proposed algorithm, whereas the white circles are those preliminarily estimated by the RPM algorithm. Figure 6(a) shows that the proposed algorithm accurately reconstructs the lower side of rectangular and triangular objects, and the false images outside the dielectric boundary are completely suppressed. Note that there is accuracy distortion around the ellipse target. This is because the left side of the dielectric boundary is not completely reconstructed by RPM, and thus, $\hat{\boldsymbol{r}}_{M,j}\left(\boldsymbol{q}_{M,i}\right)$ in Eq. (2) is incorrectly calculated. In particular, the computational time is less than 40 s with a Xeon 2.40 GHz processor, which is 34 times less than the time taken by the previous SAR algorithm. Furthermore, Fig. 6(b) shows the target points $\hat{\boldsymbol{r}}_M\left(\boldsymbol{q}_{M,i}\right)$ for another target case, where the same parameters are used as in the case of Fig. 6 (a). The figure shows that the wider region of the ellipse target is now reconstructed since the region of the dielectric boundary estimated by RPM is expanded in this case. Considering the whole image, the proposed algorithm offers various target boundaries such as the triangular edge or plane structure of a rectangular target. We also confirm that the proposed algorithm produces accurate images even for a noisy environment, where a signal-to-noise ratio is higher than 25dB. Moreover, part of the target boundary such as a rectangular or triangular side cannot be reconstructed. This is an inherent characteristic of an imaging algorithm using only single scattered signals. In our future work, we will enhance the imagery range using multiple scattered signals as discussed in [3].

References

1. David W. Winters Shea, Jacob D. Shea, Ernest L. Madsen, Gary R. Frank, Barry D.Van Veen,Hagness, and Susan C. Hagness, "Estimating the Breast Surface Using UWB Microwave Monostatic Backscatter Measurements," *IEEE Trans. Biomed Eng.*, vol. 55, No. 1, pp. 247-256, Jan., 2008.

2. S. Kidera, T Sakamoto, and T. Sato, "Accurate UWB Radar 3-D Imaging Algorithm for Complex Boundary without Range Points Connections," *IEEE Trans. Geosci. & Remote Sens.*,vol. 48, No. 48, pp. 1993-2004, Apr., 2010.

3. S. Kidera, T. Sakamoto, and T. Sato, "Shadow Region Imaging Algorithm Based on Aperture Synthesis with Multiple Scattered Waves for UWB Radars," *Proc. of PIERS 2009* vol. 5, No. 4,pp. 393-396, Aug, 2009.